Material Priority Engineered Metal-Polyphenol Networks: Mechanism And Platform For Multifunctionalities

Xinxiu Cheng
  Xinjiang Technical Institute of Physics and Chemistry

Yaxin Zhu
  Xinjiang Technical Institute of Physics and Chemistry

Ruofei Lu
  Xinjiang Technical Institute of Physics and Chemistry

Xiaoqiang Zhang
  Xinjiang Technical Institute of Physics and Chemistry

Na Li
  Wenzhou Institute, University of Chinese Academy of Sciences

Xingjie Zan (✉ xjzan2000@hotmail.com)
  School of Biomedical Engineering, Wenzhou Medical University

---

Abstract

Engineering the surface of materials with desired multifunctionalities is an effective way to fight against multiple adverse factors during the tissue repair process. Recently, metal-polyphenol networks (MPNs) have gained increasing attention because of their rapid and simple deposition process onto various substrates (silicon, quartz, gold and polypropylene sheets, etc.). However, the coating mechanism has not been clarified, and multifunctionalized MPNs remain unexplored. Herein, the flavonoid polyphenol procyanidin (PC) was selected to form PC-MPN coatings with Fe^{3+}, and assembly parameters, including pH, molar ratio between PC and Fe^{3+}, and material priority during coating formation, were thoroughly evaluated. We found that the material priority (addition sequence of PC and Fe^{3+}) had a great influence on the thickness of the formed PC-MPNs. Various surface techniques (e.g., ultraviolet-visible spectrophotometry, quartz crystal microbalance, X-ray photoelectron spectroscopy, atomic force microscopy, and scanning electron microscopy) were used to investigate the formation mechanism of PC-MPNs, and PC-MPNs were further engineered for multifunctionalities (fastening cellular attachment in the early stage, promoting long-term cellular proliferation, antioxidation and antibacterial activity). We believe that these findings could further reveal the coating formation mechanism of MPNs and guide the future design of MPN coatings with multifunctionalities, thereby greatly broadening their application prospects, such as in sensors, environments, drug delivery, and tissue engineering.

Introduction

The surface, as the first point of contact with other materials, has various functionalities that are critical to the performance of the material, especially with regard to implantation [1-4]. Once implanted, a series of biological events occur at the interface between implants and surrounding tissues, such as protein adsorption, cell attachment, infection, inflammation, or coagulation [5-8]. In fact, implantation is a complicated process that is orchestrated by various cellular and biomolecular signals in a spatiotemporally defined manner to achieve the expected outcomes [9, 10]. Engineering the surface of implants with desired multifunctionalities has been proposed as an effective way to fight against multiple adverse factors during the tissue repair process [11-14]. For example, orthopedic implants with antibacterial properties, enhanced tissue integration ability and improved bone regeneration capacity are of great interest for reducing the current high failure rate [5] (approximately 20% after 10 years of implantation based on multicenter data), which may be caused by multiple factors, such as infection, poor biocompatibility, and slow or incomplete bone regeneration [8]. However, developing a multifunctional coating based on a simple and general method remains a significant challenge.

Metal-polyphenol networks (MPNs), constructed from the dynamic coordination interactions between metal ions and phenolic ligands, have gained increasing attention since they were first reported by Caruso et al. [15] because of their rapid and simple deposition process onto various substrates with different shapes. Recently, pioneering explorations of multifunctional coatings for MPNs have been performed due to their ability to combine the functions of polyphenol and metal ions, which allows the functionalities of the formed coating to be endowed or synergistically promoted by the applied polyphenol and metal

ions. Huang et al. [16] investigated whether a film formed by polyphenol (tannic acid)/catecholamine (dopamine or norepinephrine) and copper ions could be used as a potential coating for blood-contacting implantable devices because of its synergistic anti-inflammatory, antimicrobial and anticoagulant properties. Taking advantage of the coating formed by epigallocatechin gallate (EGCG) and magnesium ions, Wang and colleagues [17] demonstrated its ability to enhance corrosive resistance and endothelialization for potential cardiovascular applications, and the Shin group [18] showed that the coating had a promising ability to promote osseointegration and bone formation and thus represented a reliable surface modification on orthopedic implants. To understand the assembly process and provide theoretical support for broad applications, the formation mechanism of MPNs has been extensively investigated, which could be influenced by many factors, such as the pH [15], solvents [19], precursor concentration [19], molar ratio between polyphenols and metal ions [15], and even the addition sequence of polyphenols and metal ions [20, 21]. However, in most current reports, the formation mechanism of MPNs is based on tannic acid (TA) [22], which is the tip of the iceberg considering the large families of polyphenols (more than 8000 species of polyphenols have been identified) [23, 24], In a recent report, Caruso et al. demonstrated that a small change in the number of possible chelating sites of polyphenols with metal ions resulted in profound formation of MPNs [25]. Considering the large number of polyphenols and the wide range of appliable metal ions (Fe^{3+}, Cu^{2+}, Mg^{2+}, etc.) [26], it is reasonable to envision that the functionality word of MPNs urgently must be developed, and the formation mechanism of MPNs is far from being fully understood.

Polyphenols, based on their carbon backbone structure, can be categorized into four kinds, phenolic acids, flavonoids, stilbenes and lignans, among which phenolic acids and flavonoids are more common [23, 27, 28]. Compared with TA (a representative phenolic acid polyphenol with a C6-C1 structure) [24], which is a model polyphenol that is typically used to study the formation mechanism of MPNs, procyanidin (PC, a homolog to flavonoid polyphenol, with a C6-C3-C6 structure, **Scheme 1a**) [24, 29], has rarely been investigated. PC is widely present in nature, especially in seeds, fruits, flowers, bark, nuts and vegetables, and exhibits excellent bioactivities, such as antioxidant activity [30], antibacterial activity [31], insect pest resistance [32], antiobesity activity [33], antithrombosis activity [34], bone osteogenesis promotion activity [35] and platelet activity modulation ability [36]. Herein, PC and iron ions (Fe^{3+}, the classic metal ions of MPNs) were chosen to investigate the ability of PC to construct MPNs (PC-MPNs) by exploring the factors affecting MPN formation and the multifunctionality of PC-MPNs. We surprisingly found that the thickness of PC-MPNs was greatly affected by the pH and molar ratio of PC to metal ions (Fe^{3+}) and by the sequence in which PC and Fe^{3+} were added. With a focus on the addition sequence of PC and Fe^{3+}, we thoroughly explored the formation mechanism of PC-MPNs and further engineered PC-MPNs for specific multifunctionalities, including accelerated cellular attachment and proliferation, strong antioxidant ability, and antibacterial ability. We believe that our findings on the PC-MPN coating formation mechanism could guide the future design of other MPN coatings and suggest that the strategy of engineering a PC-MPN coating multifunctional platform has considerable application prospects.

Materials And Methods

Materials.

Proanthocyanidin (PC), iron(III) nitrate nonahydrate ($Fe(NO_3)_3 \cdot 9H_2O$), N-2-hydroxyethyl piperazine-N'-2-sodium sulfonate salt (HEPES-Na), bis-(2-hydroxyethyl)amino-tris(hydroxymethyl)methane (bis-tris), silver nitrate ($Ag(NO_3)_3$) and tris(hydroxymethyl)aminomethane (tris) were purchased from Macklin. $NH_3 \cdot H_2O$, H_2SO_4, H_2O_2 (30%), phosphate-buffered saline (PBS), 4',6-diamidino-2-phenylindole (DAPI), rhodamine phalloidin (phalloidin-TRITC) and polypropylene (PP) sheets were purchased from Sigma. Four percent paraformaldehyde and Triton X-100 were purchased from Solarbio Life Science. Cell Counting Kit-8 (CCK-8) was obtained from Dojindo Laboratories. The ROS assay kit and ferric reducing antioxidant power (FRAP) assay kit were purchased from Beyotime Institute of Biotechnology. All chemicals were used without any further purification. Silicon wafers (SSPs), quartz plates (Alfa Aesar), and round glass coverslips (14 mm diameter from NEST) were cleaned by a piranha solution (70% H_2SO_4 and 30% H_2O_2, V/V) at 98 °C for 2 h, rinsed with Milli-Q water and subsequently dried under a mild stream of air before use (Caution: Piranha solution is highly oxidizing and corrosive, and extreme care should be taken during preparation and use). The deionized (DI) water used here was purified through a Milli-Q system and possessed a resistivity greater than 18.25 MΩ·cm.

Preparation of PC-MPN coating.

PC was dissolved in water at a concentration of 1 mM, and NaOH (2 M) was dropped into the above PC solution to adjust the pH to 8. Equal volumes of mixed buffer (pH 6.5) containing bis-tris (0.3 M) and tris (0.3 M) were added to the PC solution (1 mM, pH 8). The resulting solution was evenly mixed and subsequently centrifuged at 8600 rpm for 7 min to remove undissolved PC, and it was denoted as the mother liquid. $Fe(NO_3)_3$ solution (5 mM) was obtained by dissolving $Fe(NO_3)_3$ in water. PC-MPNs could be coated through two routes (depending on the priority of the first added material), as illustrated in **Scheme 1**b. PC-MPN coatings engineered by route I (PC priority) and route II (Fe^{3+} priority) were denoted PC-MPN^I and PC-MPN^{II}, respectively. Fabricating PC-MPN^I coating was carried out in a 10 mL tube containing a substrate (clean silicon, quartz or PP sheet with 1 cm × 1 cm), in which 1.4 mL of mother liquid was added, and then 0.7 mL of $Fe(NO_3)_3$ solution was immediately added (less than 10 s). The mixture was vigorously vortexed for 30 s, and the substrate was washed with HEPES buffer solution (0.025 M, ca. pH 8) and DI water. The substrate was then dried by a mild stream of air. The above deposition procedure of PC-MPNs was cycled until the desired thickness was obtained. The PC-MPN^{II} coating was produced by the same protocol, except that $Fe(NO_3)_3$ solution was first added followed by the addition of mother liquid. All as-prepared PC-MPN coatings were stored in a refrigerator for subsequent experiments.

Factors of PC-MPN fabrication.

The effects of the pH and molar ratio of PC to Fe^{3+} (PC:Fe^{3+}) PC-MPN fabrication were evaluated on a PC-MPN^I coating. For the pH factor, HCl or NaOH was used to adjust the pH values of the mother liquid to the setup point of 6, 7 and 8. It should be noted that the pH had no variation during the whole coating process, regardless of the addition of the $Fe(NO_3)_3$ solution due to the effect of buffer molecules in mother liquid. For the PC:Fe^{3+} factor, different ratios (1:2-1:10) were obtained by fixing the PC concentration with varying concentrations of $Fe(NO_3)_3$ solution. PC-MPN^I coatings at different pH values or different PC:Fe^{3+} ratios were obtained by the above protocol.

Deposition process of PC-MPN^I and PC-MPN^{II} coatings.

The deposition process of the PC-MPN^I and PC-MPN^{II} coatings was recorded by ultraviolet–visible (UV-vis) spectrophotometry. UV-vis spectra of the coating deposited on quartz slides were collected on a UV-vis spectrophotometer (Lambda 25, PerkinElmer). PC-MPN^I and PC-MPN^{II} coatings were coated onto quartz slides using a modified protocol, with the quartz slide washed and dried after each addition of mother liquid and $Fe(NO_3)_3$ solution. The absorbance at 200-800 nm was recorded for further analysis. The time of quartz slide immersion into mother liquid or $Fe(NO_3)_3$ solution was set at 10 s.

Decomposition process of PC-MPNs.

Generally, the decomposition process of PC-MPNs was carried out by immersing a substrate coated with PC-MPNs into an $Fe(NO_3)_3$ solution (pH 2.6) or dilute HCl solution (pH 2.6) for the desired time (5 min and 30 min). After thorough washing and careful drying, the absorbance at 200-800 nm and the thickness and morphology of these coatings were recorded by UV-vis, ellipsometry and atomic force microscopy (AFM). The thickness was approximately 14 nm for both PC-MPN^I and PC-MPN^{II} coatings, and the MPNs were fabricated by 4 cyclic depositions for the PC-MPN^I coating and 20 cyclic depositions for the PC-MPN^{II} coating.

Quartz crystal microbalance with dissipation (QCM-D) test.

The QCM-D test was performed using a Q-sense system (Biolin Scientific, Sweden) with an E4 channel to further investigate the decomposition process of the coating. The gold-coated quartz crystals for QCM measurements were cleaned in an ammonium peroxide mixture (5:1:1, water: NH_3(25%): H_2O_2 (30%)) at 75 °C for 0.5 h, rinsed with Milli-Q water, and dried with a mild stream of air [37]. The shifts in energy dissipation (ΔD) and resonance frequency (ΔF) were monitored in real time under third overtones. For the study of the coating behavior in PC solution, the coating was first prepared on QCM-D resonators with seven deposition cycles. Then, the PC solution was injected into the cells for 40 min. Following PC adsorption, rinsing solutions of bis-tris buffer and Milli-Q water were injected for 10 min each. A flow rate of 50 μL per min was maintained for every step. The study of the coating behavior in $Fe(NO_3)_3$ and HCl solutions was performed using the same protocol, except that $Fe(NO_3)_3$ and HCl solutions were injected

into the cells for 40 min to allow for adsorption. Next, rinsing solutions of Milli-Q water were injected for 10 min.

Characterization.

The thickness of the coating in the dry state was determined by optical ellipsometry (M-2000UI, J.A. Woollam). The surface morphology was observed by AFM (Dimension Icon, Bruker) in tapping mode and SEM (SU8010, HITACHI) in SE (L) mode. X-ray photoelectron spectroscopy (XPS) spectra were obtained on a Thermo-Electron ESCALAB 250 spectrometer equipped with a monochromatic Al X-ray source (1486.6 eV). Water contact angle (WCA) analyses were carried out using the static sessile drop method on a KRUSS DSA1 version 1.80 drop shape analyzer, with water as the probe liquid. Each contact angle value represented the average of at least seven measurements.

FRAP text.

The working curve was obtained first based on the protocol from the FRAP assay kit **(Fig. S1)**. In brief, 27.8 mg $FeSO_4$ solutions with different specific concentrations (0, 0.15, 0.3, 0.6, 0.9, 1.2 and 1.5 mM) were prepared and injected into a 96-well plate, into which working solution (180 μL) was added. After incubating for 5 min at 37 °C, the 96-well plate was read at 593 nm with a spectrophotometer. The total antioxidant activities of the PC-MPN$^{\square}$ coatings were measured with the same procedure, except that the PC-MPN$^{\square}$ coatings or glass were used instead of the $FeSO_4$ solution for reacting with the FRAP working solution. After reacting for 5 min at 37 °C, the samples were taken out, and the solution was read by a spectrophotometer at 593 nm. Based on the tested intensity, the antioxidant activity of each sample was calibrated from the standard curve. After 3 repetitions, the average data were reported.

Cell culture.

MC3T3-E1 cells (ATCC, subclone 14) were cultured and passaged onto a 75 mm^2 tissue culture flask at 37 °C in humidified air containing 5% CO_2 supplemented with Dulbecco's modified Eagle's medium (DMEM) supplemented with 10% fetal bovine serum, penicillin 100 (units/mL) and streptomycin (100 μg/mL).

Cell attachment and spreading at early stage.

MC3T3-E1 cells were collected and redispersed in culture medium. After counting the number of cells, MC3T3-E1 cells were seeded on glass coverslips with or without PC-MPN$^{\square}$ coatings at a density of 4×10^4 cells/cm^2. At 2 and 4 h after seeding, the glass coverslips were taken out and washed softly with PBS, and then the cells were fixed by immersion in 4% paraformaldehyde for 30 min. The coverslips were further treated with PBS containing 0.2% (v/v) Triton X-100 for 10 min, followed by rinsing with PBS five times. Then, all coverslips were stained subsequently with actin filaments with the fluorescent dye phalloidin-TRITC (red), and nuclei were stained with DAPI (blue). The cell morphology was imaged by fluorescence microscopy (DMi8, Leica).

Cell proliferation.

Cell proliferation was tested on PC-MPN$^{\square}$ coatings by seeding MC3T3-E1 cells at a density of 1×10^4 cells/cm^2 in 24-well plates, with glass used as the control. After culturing for several days (1, 3 and 7 days), a CCK-8 kit was used to test the viability of cells with the procedure from the kit. Briefly, CCK-8 solution (10% of the total medium volume) was added to MC3T3-E1 cells. After 2 h of incubation, 100 μL aliquots from each sample were transferred to a 96-well plate and read at 450 nm. The data are reported as the average value from triplicates. After culturing for 7 days, the cells were fixed and stained by the previous procedure and imaged by fluorescence microscopy.

Intracellular ROS level.

MC3T3-E1 cells were seeded on coated glass coverslips at a density of 4×10^4 cells/cm^2. After 24 h of culture, the medium was replaced by DMEM with/without 10 mM H_2O_2. After 2 h of culture, the cells were washed gently with PBS 3 times. Cells were stained by the previous procedure and imaged by fluorescence microscopy.

Antibacterial test.

Bacteria (*S. aureus* (ATCC #6538) and *E. coli* (ATCC #8739)) in lysogeny broth (LB) medium were harvested by centrifugation and resuspended in PBS buffer solutions (pH 7.2) to a final concentration of 1×10^8 in 10 mL solution. The PC-MPN$^{\square}$ coating was immersed in a $Ag(NO_3)_3$ solution (10 mM) for 24 h to obtain the PC-MPN$^{\square}$-Ag coating. The samples (PC-MPN$^{\square}$ and PC-MPN$^{\square}$-Ag coatings) and the control (bare silicon wafer and glass) were immersed in 1 mL of the above bacterial solution in 24-well plates and incubated for another 6 h at 37 °C. Then, the samples and the control were washed three times with PBS. For the silicon wafer group, the sample substrates were immersed in paraformaldehyde (4%) for 15 min for prefixation and subsequently washed three times with PBS. After the samples and the control were dried under vacuum, field scanning electron microscopy (SEM) measurements were carried out to observe the morphological change in the bacterial cells. A LIVE/DEAD BacLight kit was used to further test the antibacterial ability of samples, where live and dead bacteria were stained green and red, respectively. The procedure was followed using the protocol provided by the kit. Finally, the morphological changes in the bacterial cells were imaged by confocal laser scanning microscopy (CLSM, A1 Nikon).

Data processing and statistical analysis.

All data were reported as the average of at least three duplicates, with the error bar indicating the standard deviation. At least 3 randomly selected images were obtained to analyze the cell number and cell area with ImageJ, which was downloaded from its official website (https://imagej.net/downloads). Statistical analyses were performed using the t-test, and significance was noted as "*", "**", "***" and "****" for p<0.05, p<0.01, p<0.001 and p<0.0001, respectively. No significance was noted as "ns".

Results And Discussion

PC-MPNs could be successfully coated onto bare substrates through two routes depending on the priority of PC or Fe: route I, in which PC solution was added first followed by Fe^{3+}; and route II, in which Fe^{3+} solution was added first followed by PC. To understand the deposition mechanism of PC-MPNs, factors that affect the growth behavior of PC-MPNs, including the pH, molar ratio between PC and Fe^{3+}, and different routes (route I and route II in **Scheme 1b**), were investigated. To avoid the interplay between these factors, only one factor was tested, while the other factors remained unchanged. As displayed in **Fig. 1**a, in pH 6.5 buffer, the thickness of the PC-MPN^I coating gradually increased within increasing tested molar ratio range from 1:2 to 1:10, and a further increase in Fe^{3+} led to a plateaued thickness. As shown in **Fig. 1**b, under a fixed molar ratio of 1:10, the thickness of the PC-MPN^I coating decreased when the pH value increased from pH 6 to 8, which may be due to the weak interaction between PC and the substrate at high pH, thus making it difficult to form an MPN coating. Using an optimized molar ratio (PC:Fe^{3+}, 1:10) and pH 6.5, the engineering routes (route I and route II) for the PC-MPN coating were inspected. We found that the growth of the PC-MPN coating was greatly affected by the engineering route (route I and route II). As shown in **Fig. 1**c, the PC-MPN^I coating showed fast linear growth of approximately 31 nm after seven deposition cycles, with approximately 4-5 nm per cycle. In contrast, the PC-MPN^{II} coating displayed very slow growth at less than 6 nm over seven deposition cycles, with less than 1 nm in each cycle. The growth of the PC-MPN^I coating was approximately 5 times faster than that of the PC-MPN^{II} coating.

To further investigate the efficiency of the two assembly coatings, PC-MPNs were coated onto transparent PP sheets. This efficiency can be clearly observed from the color change in **Fig. 1**d. Compared with the PC-MPN^{II} coating, the color of the PC-MPN^I coating deepened more significantly as the number of deposition cycles increased; moreover, route I was much more effective than route II for PC-MPN coating formation. This finding could also be verified from the changes in the WCA. Due to the hydrophilicity of PC, the WCA of PP sheets decreased when the PC-MPN coating formed (**Fig. 1**e). The decreasing rate of the PC-MPN^I coating was much faster than that of the PC-MPN^{II} coating with increasing number of cycles, and the WCA of the PC-MPN^I coating was much lower than that of the PC-MPN^{II} coating at the same number of cycles. The WCA of the PC-MPN^I coating decreased to flat (approximately 18 degrees) at a deposition cycle number of 10, while it was far beyond the terrace for the PC-MPN^{II} coating (approximately 77 degrees).

For PC-MPNs coated on a bare silicon wafer by route I and route II, the presence of Fe_{2p} signals indicated the successful deposition of PC-MPNs, as tested by XPS (**Fig. 1**f), which is a technique sensitive to several nanometers of surface. The Si_{2p} signal from the underlying substrate was clearly detected in the PC-MPN^{II} coating (**Fig. 1**f, top) but not in the PC-MPN^I coating (**Fig. 1**f, bottom), suggesting a thicker coating formed by the PC-MPN^I coating. All these data (**Figs. 1**c-1f) indicated that route I was much more effective than route II in fabricating PC-MPN coatings. In the following, the chemical composition and the constructive mode of the PC-MPN^I and PC-MPN^{II} coatings were investigated by XPS, and more than one hundred cycles were deposited onto silicon to avoid disturbance of the underlying substrate (**Fig. S2**).

As expected, the silicon signal disappeared for both the PC-MPN^{I} and PC-MPN^{II} coatings, suggesting that the XPS signals originated from the coatings (**Fig. S2**). In the detailed Fe_{2p} spectra (**Fig. 2**a), two split peaks at 725 eV and 712 eV were observed, indicating the presence of Fe^{3+} in both PC-MPN^{I} and PC-MPN^{II} coatings. The atomic percentages of carbon (C), oxygen (O) and iron (Fe) are illustrated in **Fig. 2**b, and no large difference between PC-MPN^{I} and PC-MPN^{II} coatings was observed, except for the slight increase in Fe content (1.9% in PC-MPN^{I} coating and 2.3% in PC-MPN^{II} coating). Furthermore, the generated molar ratios of Fe to PC in PC-MPN^{I} and PC-MPN^{II} coatings were 0.98 and 1.15 (**Fig. 2**c), respectively. In the detailed O 1s spectra (**Fig. 2**d of PC-MPN^{I} coating and **Fig. 2**e of PC-MPN^{II} coating), three peaks were observed: Fe-O [38, 39] (coordination bond between PC and Fe) at 531.2 eV, O-C in PC at 532.5 eV and Fe-OH [22, 40] (hydrogen bonding interaction between PC and Fe) at 533 eV. After the peak fit, the proportion of O in different states was obtained. As shown in **Fig. 2**f, compared to the PC-MPN^{I} coating, the PC-MPN^{II} coating had a higher proportion of coordinative bonds (53% in the PC-MPN^{II} coating vs. 42% in the PC-MPN^{I} coating) but a lower proportion of O-C bonds (26% in the PC-MPN^{II} coating vs. 34% in the PC-MPN^{I} coating), suggesting more coordinative interactions and less PC in the PC-MPN^{II} coating. Overall, these two coatings had almost the same chemical composition and were constructed by similar modes but different proportions in constructive mode.

To further investigate the reasons for the above differences (coating efficiency and constructive mode) between the PC-MPN^{I} and PC-MPN^{II} coatings, UV-vis was utilized to observe the engineering steps in each cycle, and the absorbance at 210 nm associated with the absorption of phenyl groups in PC was used to quantify the PC in the coating (**Figs. S**3, **S**4).

For the PC-MPN^{I} coating (**Fig. 3**a), there was a continuous increase in absorbance at 210 nm every step in each cycle, regardless of whether PC or Fe^{3+} was added. However, the PC-MPN^{II} coating exhibited a zigzag-type increase (**Fig. 3**b), with an increase in the step of adding PC but a decrease in the step of adding Fe^{3+}, which was totally different from the growth profile of the PC-MPN^{I} coating. In addition, the absorbance of the PC-MPN^{II} coating was much lower than that of the PC-MPN^{I} coating at the same number of deposition cycles. These data (**Figs. 3**a, b) suggested that although the PC-MPN coating can be generated by both route I and route II, PC-MPN^{I} was much more efficient than PC-MPN^{II}, which was consistent with the above thickness test (**Fig. 1**c). The low coating efficiency of PC-MPN^{II} was attributed to the decomposition of predeposited PC-MPNs during the step of adding Fe^{3+}, and only 40% of the newly deposited coating in the last cycle was retained (**Fig. S5**, deduced from the data in **Fig. 3**b). Next, the decomposition process of preformed PC-MPNs induced by Fe^{3+} was explored to deeply understand the formation mechanism of the PC-MPN coating. Considering that the MPNs are extremely sensitive to acidic environments and that the $Fe(NO_3)_3$ solution used here was pH 2.6, a PC-MPN^{II} coating with a thickness of approximately 14 nm was separately immersed into dilute HCl at pH 2.6 and $Fe(NO_3)_3$ solutions for 5 min to reveal the roles of acidic environments and Fe^{3+} in this decomposition process. UV-vis was recorded before and after immersion (**Fig. S6**). Decreased

absorbance was found after both treatments, and the $Fe(NO_3)_3$ treatment resulted in a greater decrease than the dilute HCl treatment (**Fig. 3**c). The thickness change in the PC-MPN^{II} coating by the same treatment could support UV-vis data. As exhibited in **Fig. 3**d, treatment with $Fe(NO_3)_3$ led to a greater decrease in thickness than treatment with dilute HCl. The average decomposition rate could be calculated based on the data in **Figs. 3**c, d. The decomposition rate induced by $Fe(NO_3)_3$ was approximately 2.2 times faster than that induced by dilute HCl based on the UV-vis data in **Fig. 3**c**,** and it was approximately 2.4 times faster based on the thickness data in **Fig. 3**d. The faster decomposition rate by $Fe(NO_3)_3$ may be attributed to the excessive Fe^{3+} competing with the PC in the preformed coating in an acidic environment, which resulted in faster destruction of PC-MPNs. These data strongly showed that both an acidic environment and Fe^{3+} played a role in breaking the predeposited PC-MPN coating.

Then, QCM-D, a real-time observation technique with sensitivity to a picometer of the coating on its sensor, was performed to investigate this decomposition process. After injecting dilute HCl or $Fe(NO_3)_3$ into the chamber in which the PC-MPN^{II} coating was coated onto the sensor, the frequency significantly increased with time (**Fig. 3**e), suggesting decomposition of the PC-MPN coating. Compared to dilute HCl, $Fe(NO_3)_3$ showed a faster decomposition rate, especially in the first 5 min, which was consistent with the UV-vis observations. In addition, $Fe(NO_3)_3$ experienced a quicker equilibrium process with less decomposed material than dilute HCl. In contrast, the injection of PC resulted in a continuously decreased frequency (**Fig. 3**f), suggesting the deposition of PC onto the PC-MPN coating. Obviously, during engineering of the PC-MPN^{I} and PC-MPN^{II} coatings, the total performance of $Fe(NO_3)_3$ and PC on the PC-MPN coating leads to different coating efficiencies and constructive modes of the MPN coating.

The stability of the PC-MPN^{I} and PC-MPN^{II} coatings was further checked by immersing them into $Fe(NO_3)_3$ solution for 30 min. As displayed in **Fig. 4**a, from the original similar thickness (~14 nm), the thickness of both PC-MPN^{I} and PC-MPN^{II} coatings decreased. Compared to the PC-MPN^{II} coating, the PC-MPN^{I} coating showed a much smaller decrease, which was further proven by the percent of reserved thickness (**Fig. S7**). More than 98% of the coating was reserved for PC-MPN^{I}, while only 75% was left for PC-MPN^{II}.

The morphologies of these coatings before and after immersion in $Fe(NO_3)_3$ solution for 30 min were recorded by AFM, which is a technique sensitive to the surface. As shown in **Figs. 4**b, c, all coatings were uniform and presented a particle-like height structure on the surface, both before and after immersion. The morphology of the PC-MPN^{I} coating seemed flatter than that of the PC-MPN^{II} coating (**Fig. 4**b vs. **Fig. 4**c), and the height structure of the PC-MPN^{II} coating decreased obviously after immersion (**Fig. 4**c_1 vs. **Fig. 4**c_2). The roughness of the PC-MPN^{I} coating had no obvious change before and after immersion (**Fig. 4**d). There was a significant decrease in the PC-MPN^{II} coating after immersion (**Fig. 4**d). All these data (**Figs. 4**a-**4**d) suggested that the PC-MPN^{I} coating was more stable than the PC-MPN^{II} coating in resisting the erosion of $Fe(NO_3)_3$.

Based on the above results, the formation mechanisms of PC-MPN^{I} and PC-MPN^{II} coatings were proposed. As illustrated in **Scheme 2**a for producing the PC-MPN^{I} coating, adding PC first led to PC deposition onto the preformed PC-MPN coating and increased the thickness, and the subsequent addition of Fe^{3+} contributed to a further thickness increase by assembly with the predeposited PC; meanwhile, the complex of PC and Fe^{3+} in solution was further deposited onto the PC-MPN coating. According to the generation of the PC-MPN^{II} coating in **Scheme 2**b, adding Fe^{3+} first resulted in the decomposition of the preformed PC-MPN coating, and adding PC second led to the deposition of PC onto the substrate and the formation of the complex of PC and Fe^{3+} in solution, which could be further deposited onto the substrate. The cause of the decomposition of the PC-MPN coating by Fe^{3+} priority was that the dynamic coordinative balance between PC and Fe^{3+} in the coating was broken by the low pH and presence of Fe^{3+}. Compared with the Fe^{3+} priority, the PC priority did not result in decomposition of the preformed PC-MPN coating, but the deposition might be the hydrophobic interaction and hydrogen bonding between PC in PC-MPNs and PC in solution. Further deposition of the PC and Fe^{3+} complex onto the substrate could be supported by the SEM images and roughness of the coating (**Figs. S8**, S**9**). As exhibited in **Fig. S8**, the number of particles on the surface of both PC-MPN^{I} and PC-MPN^{II} coatings obviously increased with increasing number of deposition cycles. In **Fig. S9**, the roughness tested by AFM increased with increasing number of deposition cycles. It is worth noting that the PC-MPN^{I} coating had a higher roughness than the PC-MPN^{II} coating with the same number of deposition cycles.

It is worth noting that the phenomena of the material priority-dominated PC-MPN coating were opposite to those of the most studied TA-MPN coating, in which the priority of Fe^{3+} resulted in an efficient process while the priority of polyphenol TA was an inefficient coating route.[20, 21] This might be mainly attributed to the difference in backbone between phenolic acids (TA, C6-C1) and flavonoids (PC, C6-C3-C6) and the different applied pH values during MPN formation.

Because of the multifunctionality presented by PC (antioxidant, antibacterial, insect pest resistance, antiobesity, etc.), the performance of PC-MPNs as a bioactive interface platform was investigated. In the following studies, only PC-MPN^{I} coating was utilized to coat the substrate due to its high coating efficiency and relative stability. The antioxidant activity of the PC-MPN coating was first evaluated by the FRAP assay.. Based on the tested intensity, the antioxidant activity of each sample was calibrated from the standard curve (**Fig. S1**). Glass was run as a control group. The antioxidant activities were revealed in the short term and the long term by testing the antioxidant activities of the PC-MPN coating at different time intervals (i.e., freshly prepared and stored for 1, 3, and 5 weeks). As shown in **Fig. 5**, the PC-MPN coating exhibited much higher antioxidant activity than the glass control, which demonstrated that the coating was responsible for the antioxidant activity of the samples. Although the antioxidant activity decreased after preparation due to the oxidized effect of oxygen in the air on PC, there was no obvious difference until the tested 3 weeks, which is critical for future clinical applications.

The early and long-term adhesion of cells on the surface of materials is an important index for evaluating the effect of the interaction between materials and cells. Quick cell attachment and spreading onto

implants at an early stage are beneficial for integrating tissue cells and mitigating the effect of bacteria [41-44]. Cell attachment onto the PC-MPN coating at an early stage was observed by fluorescence images of the behavior of MC3T3-E1 cells at 2 h and 4 h after seeding, and the cells seeded on glass were used as the control. As shown in **Fig. 6**a, b, the cells on the surface of the PC-MPN coating exhibited slight dispersal and showed a well-defined morphology at both 2 h and 4 h, while the cells on glass were round at 2 h and slightly spread at 4 h.

In a further analysis, the cell number and cell area per square millimeter, which are two of the most important indices for evaluating attachment at an early stage, were also quantified, as plotted in **Figs. 6**c, d. Obviously, compared with that at 2 h, both the cell number and cell area per square millimeter further increased at 4 h for all samples. Significantly, more cells adhered to the PC-MPN coating than glass at both 2 h and 4 h. The cell numbers on the coating were all 1.3-fold higher than those on glass at both 2 h and 4 h (**Fig. 6**c). For the area per square millimeter (**Fig. 6**d), cells on the PC-MPN coating also had a higher area than that on glass, and the values were 1.78-fold and 1.44-fold higher than that on glass at both 2 h and 4 h, respectively. All the above results showed that the PC-MPN coating provided a microenvironment for the rapid attachment and dispersal of MC3T3-E1 cells at an early stage.

To investigate the proliferation of MC3T3-E1 cells on PC-MPN coatings, a longer culture time was carried out, and cell viability (an indicator of cell numbers) was tested on days 1, 3, and 7. The number of proliferated cells was evaluated from the OD values of the CCK-8 assay, which was based on dehydrogenase activity detection in viable cells to count the number of cells. The OD value of the CCK-8 assay was proportional to the number of viable cells. With the cell viability on glass at day 1 as the control, the cellular viabilities are shown in **Fig. 7**a. Obviously, the cell viabilities increased with culture time for all samples, suggesting that all seeded cells settled on all samples in a similar way and began proliferating normally. At any culturing time, the number of cells on the coating was higher than that on glass, demonstrating the good proliferation of cells on the PC-MPN coating. On the 7th day, the cells were stained and imaged (**Fig. 7**b). Furthermore, the cell numbers were counted based on the number of cellular nuclei in **Fig. 7**b and are displayed in **Fig. 7**c. Clearly, we observed that a higher number of cells adhered to the PC-MPN coating than glass after 7 days of culture, which was consistent with the CCK-8 assay (**Fig. 7**a). In detail, the cell viability on the PC-MPN coating was approximately 1.7 times higher than that on glass at the same time point. Considering the infinite cell numbers under in vivo conditions, these features of fast cell attachment and spreading at an early stage and proliferation in the initial days indicate that the PC-MPN coating is a good candidate for attracting more cells to attach, spread and proliferate.

Because PC has good antioxidant activity, especially after chelation with metal ions under suitable conditions [30, 45], a PC-MPN coating was chosen to further investigate the antioxidant properties of the cell response. To simulate an overstressed ROS environment [46, 47], 10 mM H_2O_2 was added to the culture medium as an ROS provider. As displayed in the top panel of **Figs. 8**a, b, the cells had extensively spread onto all samples before H_2O_2 treatment. After treatment with H_2O_2 for 20 min (bottom panel of **Figs. 8**a, b), the cells on glass became skinny, and the number of attached cells decreased accordingly.

Interestingly, although the cell area and number of cells that adhered to the coating also changed after H_2O_2 treatment, the trend of change was slighter than that of the glass. Further analysis of the difference was quantified by counting the number of cells and measuring the cell area per square millimeter. As displayed in **Fig. 8**c, the cell number per square millimeter on glass exhibited a sudden decrease, with more than 89% of the original attached cells lost after H_2O_2 treatment. As a comparison, more than 80% of the original attached cells remained attached to the coating. The cell area per square millimeter is plotted in **Fig. 8**d, and a decreased area was observed for all samples. However, the area of decrease was 93% and 10% for glass and the coating, respectively. Evidently, cells attached to the PC-MPN coating had a stronger ability to resist oxidative stress than those on glass.

Bacterial infections, especially in connection with the use of medical diagnostic devices and therapeutic tools/implants, are among the main causes of death worldwide [8]. To address the issue of infections, effective antibacterial materials are still highly sought. Since both polyphenols [31, 48-50] and iron [51, 52] have the ability to kill bacteria, we next tested the antibacterial properties of the coating. The ability of the PC-MPN coating to kill bacteria was tested by immersing the coating into bacterial solutions and then comparing the deformed and collapsed bacteria to those on the silicon wafer control. To show the power of the coating to kill bacteria, two bacteria were chosen as representatives: *S. aureus*, which represents gram-positive bacteria, and *E. coli*, which represents gram-negative bacteria. We employed SEM to characterize the antibacterial activity of the PC-MPN coating. As vividly displayed in **Fig. 9**a, on the control silicon wafer, cells of *S. aureus* appeared intact, had a round shape and tended to form colonies with each other. No visible abnormalities were observed. However, bacteria in contact with the PC-MPN coating showed deformation, collapsed bacterial structures and fusion of the bacterial membrane; in addition, islands with ruptured bacteria occurred, thus revealing severe damage to the bacterial structure. Cells of *E. coli* appeared to have similar results to those for *S. aureus*. Notably, Ag^+ is well known for its multilevel antimicrobial mode, even at very low concentration levels, which ensures wide-spectrum and long-term antibacterial characteristics. Taking the reducing ability of residual phenolic hydroxyl groups on the PC-MPN coating, silver ions can be reduced to silver nanoparticles in situ with good antibacterial activity. Furthermore, we also explored the antibacterial properties of the PC-MPN-Ag coating. Distinctly, both *S. aureus* and *E. coli* displayed further fusion of the bacterial membrane on the PC-MPN-Ag coating, indicating that the PC-MPN-Ag coating showed stronger bactericidal ability (**Fig. 9**a).

To further confirm the antibacterial activity, the SYTO 9/PI method was implemented, with dead bacteria dyed red and live bacteria dyed green. As displayed in **Fig. 9**b, bacteria attached to the PC-MPN and PC-MPN-Ag coatings were red, while bacteria attached to the control (glass) were green. Notably, compared with glass, the number of dead and live bacteria on the PC-MPN-Ag coating showed a decreasing tendency, especially for *E. coli*, which may be due to the strong antibacterial property of the PC-MPN-Ag coating preventing the bacteria from firmly adhering to the coating surface and reducing proliferation. All of these results further illustrated that the PC-MPN coating, particularly the PC-MPN-Ag coating, has strong antibacterial ability against *S. aureus* and *E. coli*.

Conclusions

In summary, we successfully engineered flavonoid-based multifunctional MPNs constructed from PC and Fe^{3+}. The desired PC-MPN coating was obtained by optimizing assembly parameters, such as pH, polyphenol-to-metal molar ratio and polyphenol-to-metal priority in each deposition cycle. For the PC priority (PC-MPN^I), the growth rate was 5 times faster than that of the Fe^{3+} priority (PC-MPN^{II}). The attachment of PC onto the substrate or preformed PC-MPN coating was critical to the continuous and accelerated growth of the PC-MPN^I coating, while the decomposition of dilute HCl and Fe^{3+} led to a zigzag pattern and slower growth of the PC-MPN^{II} coating. In addition to the high coating efficiency, the PC-MPN^I coating exhibited a higher stability in terms of resistance to Fe^{3+} erosion than the PC-MPN^{II} coating. Furthermore, the PC-MPN coating greatly promoted cell adhesion and proliferation and antioxidative and antibacterial activities. We believe that these findings could reveal the formation mechanism of MPNs and be helpful for the future design of MPN-related coatings, and the strategy of engineering PC-MPN coatings with multifunctionalities could pave the way to considerable applications, such as in sensors, the environment, drug delivery, and tissue engineering.

Declarations

Availability of data and materials

The datasets used and analyzed during the current study are available from the corresponding author on reasonable request.

Ethics approval and consent to participate

Not applicable.

Consent for publication

All authors are agreed to publish this paper.

Competing interests

The authors declare no conflict of interest.

Author details

§Xinjiang Technical Institute of Physics and Chemistry, Chinese Academy of Sciences, Urumqi 830011, P.R. China. ¶School of Ophthalmology and Optometry, Eye Hospital, School of Biomedical Engineering, Wenzhou Medical University 270 Xueyuan Road, Wenzhou 325035, P.R. China. †Oujiang Laboratory, Wenzhou Institute, University of Chinese Academy of Sciences, Wenzhou 325001, China.

References

1. Cheon KH, Park C, Kang MH, Kang IG, Lee MK, Lee H, Kim HE, Jung HD, Jang TS. Construction of tantalum/poly(ether imide) coatings on magnesium implants with both corrosion protection and osseointegration properties. Bioact Mater. 2021;6(4):1189-1200.

2. Kumari S, Tiyyagura HR, Pottathara YB, Sadasivuni KK, Ponnamma D, Douglas TEL, Skirtach AG, Mohan MK. Surface functionalization of chitosan as a coating material for orthopaedic applications: a comprehensive review. Carbohydr Polym. 2021;255:No. 117487.

3. Pazarceviren AE, Tezcaner A, Evis Z. Multifunctional natural polymer-based metallic implant surface modifications. Biointerphases. 2021;16(2):No. 020803.

4. Chen Q, Yu S, Zhang DH, Zhang WJ, Zhang HD, Zou JC, Mao ZW, Yuan Y, Gao CY, Liu RH. Impact of antifouling PEG layer on the performance of functional peptides in regulating cell behaviors. J Am Chem Soc. 2019;141(42):16772-16780.

5. Smith AJ, Dieppe P, Vernon K, Porter M, Blom AW. Failure rates of stemmed metal-on-metal hip replacements: analysis of data from the national joint registry of england and wales. Lancet. 2012;379(9822):1199-1204.

6. Yang SS, Wang Y, Luo S, Shan CJ, Geng YB, Zhang TH, Sheng SR, Zan XJ. Building polyphenol and gelatin films as implant coating, evaluating from in vitro and in vivo performances. Colloids Surf B. 2019;181:549-560.

7. Wang YK, Teng WSY, Zhang ZJ, Zhou XZ, Ye YX, Lin P, Liu A, Wu Y, Li BH, Zhang CD, et al. A trilogy antimicrobial strategy for multiple infections of orthopedic implants throughout their life cycle. Bioact Mater. 2021;6(7):1853-1866.

8. Goodman SB, Yao ZY, Keeney M, Yang F. The future of biologic coatings for orthopaedic implants. Biomaterials. 2013;34(13):3174-3183.

9. Fang Y, Guo J, Wu D, Wu LY, Song LX, Zhang Z, Zhao YS, Chang CK. Integration analysis of JAK2 or RUNX1 mutation with bone marrow blast can improve risk stratification in the patients with lower risk myelodysplastic syndrome. Front Oncol. 2021;10:No. 610525.

10. Song K, Liu N. Effect of 1,25-dihydroxyvitamin don bone marrow mesenchymal stem cells differentiation and osteoporosis through wingless-related integration site 5 (Wnt5)/tumor growth factor-beta TGF-beta signaling pathway. J Biomater Tissue Eng. 2020;10(11):1706-1712.

11. Zhang J, Ma XY, Lin D, Shi HS, Yuan Y, Tang W, Zhou HJ, Guo H, Qian JC, Liu CS. Magnesium modification of a calcium phosphate cement alters bone marrow stromal cell behavior via an integrin-mediated mechanism. Biomaterials. 2015;53:251-264.

12. Liu W, Liu C, Liu C, Li Y, Pan L, Wang J, Jian X. Surface chemical modification of poly(phthalazinone ether nitrile ketone) through RhBMP-2 and antimicrobial peptide conjugation for enhanced osteogenic and antibacterial activities in vitro and in vivo. Chem Eng J. 2021;424:No. 130321.

13. Matter MT, Maliqi L, Keevend K, Guimond S, Ng J, Armagan E, Rottmar M, Herrmann IK. One-step synthesis of versatile antimicrobial nano-architected implant coatings for hard and soft tissue healing. ACS Appl Mater Interfaces. 2021;13(28):33300-33310.

14. Del Olmo JA, Perez-Alvarez L, Pacha-Olivenza MA, Ruiz-Rubio L, Gartziandia O, Vilas-Vilela JL, Alonso JM. Antibacterial catechol-based hyaluronic acid, chitosan and poly (n-vinyl pyrrolidone) coatings onto Ti6Al4V surfaces for application as biomedical Implant. Int J Biol Macromol. 2021;183:1222-1235.

15. Ejima H, Richardson JJ, Liang K, Best JP, van Koeverden MP, Such GK, Cui JW, Caruso F. One-step assembly of coordination complexes for versatile film and particle engineering. Science. 2013;341(6142):154-157.

16. Li X, Gao P, Tan J, Xiong K, Maitz MF, Pan C, Wu H, Chen Y, Yang Z, Huang N. Assembly of metal−phenolic/catecholamine networks for synergistically anti-inflammatory, antimicrobial, and anticoagulant coatings. ACS Appl Mater Interfaces. 2018;10(47):40844-40853.

17. Zhang B, Yao RJ, Li LH, Wang YN, Luo RF, Yang L, Wang YB. Green tea polyphenol induced Mg^{2+}-rich multilayer conversion coating: toward enhanced corrosion resistance and promoted in situ endothelialization of AZ31 for potential cardiovascular applications. ACS Appl Mater Interfaces. 2019;11(44):41165-41177.

18. Lee S, Chang Y-Y, Lee J, Madhurakkat Perikamana SK, Kim EM, Jung Y-H, Yun J-H, Shin H. Surface engineering of titanium alloy using metal-polyphenol network coating with magnesium ions for improved osseointegration. Biomater Sci. 2020;8(12):3404-3417.

19. Zhong QZ, Pan SJ, Rahim MA, Yun G, Li JH, Ju Y, Lin ZX, Han YY, Ma YT, Richardson JJ, Caruso F. Spray assembly of metal-phenolic networks: formation, growth, and applications. ACS Appl Mater Interfaces. 2018;10(39):33721-33729.

20. Yang LW, Han LL, Ren J, Wei HL, Jia LY. Coating process and stability of metal-polyphenol film. Colloids Surf A Physicochem Eng Asp. 2015;484:197-205.

21. Li D, Xu X, Wang X, Li R, Cai C, Sun T, Zhao Y, Chen L, Xu J, Zhao N. General surface modification method for nanospheres via tannic acid-Fe layer-by-layer deposition: preparation of a magnetic nanocatalyst. ACS Appl Nano Mater. 2019;2(6):3510-3517.

22. Rahim MA, Ejima H, Cho KL, Kempe K, Mullner M, Best JP, Caruso F. Coordination-driven multistep assembly of metal-polyphenol films and capsules. Chem Mater. 2014;26(4):1645-1653.

23. Manach C, Scalbert A, Morand C, Remesy C, Jimenez L. Polyphenols: food sources and bioavailability. Am J Clin Nutr. 2004;79(5):727-747.

24. Bravo L. Polyphenols: chemistry, dietary sources, metabolism, and nutritional significance. Nutr Rev. 1998;56(11):317-333.

25. Lin G, Rahim MA, Leeming MG, Cortez-Jugo C, Besford QA, Ju Y, Zhong QZ, Johnston ST, Zhou JJ, Caruso F. Selective metal-phenolic assembly from complex multicomponent mixtures. ACS Appl Mater Interfaces. 2019;11(19):17714-17721.

26. Guo JL, Ping Y, Ejima H, Alt K, Meissner M, Richardson JJ, Yan Y, Peter K, von Elverfeldt D, Hagemeyer CE, Caruso F. Engineering multifunctional capsules through the assembly of metal-phenolic networks. Angew Chem Int Ed. 2014;53(22):5546-5551.

27. Xu LQ, Neoh KG, Kang ET. Natural polyphenols as versatile platforms for material engineering and surface functionalization. Prog Polym Sci. 2018;87:165-196.

28. Reitzer F, Allais M, Ball V, Meyer F. Polyphenols at interfaces. Adv Colloid Interface Sci. 2018;257:31-41.

29. Wen KS, Ruan X, Wang J, Yang L, Wei F, Zhao YX, Wang Q. Optimizing nucleophilic depolymerization of proanthocyanidins in grape seeds to dimeric proanthocyanidin b1 or b2. J Agric Food Chem. 2019;67(21):5978-5988.

30. Zhong XX, Qin BT, Dou GL, Xia C, Wang F. A chelated calcium-procyanidine-attapulgite composite inhibitor for the suppression of coal oxidation. Fuel. 2018;217:680-688.

31. Riihinen KR, Ou ZM, Godecke T, Lankin DC, Pauli GF, Wu CD. The antibiofilm activity of lingonberry flavonoids against oral pathogens is a case connected to residual complexity. Fitoterapia. 2014;97:78-86.

32. Haukioja E. Putting the insect into the birch-insect interaction. Oecologia. 2003;136(2):161-168.

33. Hou XD, Guan XQ, Cao YF, Weng ZM, Hu Q, Liu HB, Jia SN, Zang SZ, Zhou Q, Yang L, et al. Inhibition of pancreatic lipase by the constituents in St. John's Wort: in vitro and in silico investigations. Int J Biol Macromol. 2020;145:620-633.

34. Wei LH, Chen TR, Fang HB, Jin Q, Zhang SJ, Hou J, Yu Y, Dou TY, Cao YF, Guo WZ, Ge GB. Natural constituents of St. John's Wort inhibit the proteolytic activity of human thrombin. Int J Biol Macromol. 2019;134:622-630.

35. Zhu W, Yin ZQ, Zhang Q, Guo SF, Shen Y, Liu T, Liu B, Wan L, Li S, Chen X, et al. Proanthocyanidins inhibit osteoclast formation and function by inhibiting the NF-kappa B and JNK signaling pathways during osteoporosis treatment. Biochem Biophys Res Commun. 2019;509(1):294-300.

36. Rein D, Paglieroni TG, Pearson DA, Wun T, Schmitz HH, Gosselin R, Keen CL. Cocoa and wine polyphenols modulate platelet activation and function. J Nutr. 2000;130(8):2120S-2126S.

37. Zan XJ, Hoagland DA, Wang T, Peng B, Su ZH. Polyelectrolyte uptake by PEMs: impacts of molecular weight and counterion. Polymer. 2012;53(22):5109-5115.

38. Gust J, Suwalski J. Use of mssbaure-spectroscopy to study reaction-products of polyphenols and iron compounds. Corrosion. 1994;50(5):355-365.

39. Zhou YN, Xing XH, Liu ZH, Cui LW, Yu AF, Feng Q, Yang HJ. Enhanced coagulation of ferric chloride aided by tannic acid for phosphorus removal from wastewater. Chemosphere. 2008;72(2):290-298.

40. Bock CW, Markham GD, Katz AK, Glusker JP. The arrangement of first-and second-shell water molecules around metal ions: effects of charge and size. Theor Chem Acc. 2006;115(2-3):100-112.

41. Khalili AA, Ahmad MR. A Review of cell adhesion studies for biomedical and biological applications. Int J Mol Sci. 2015;16(8):18149-18184.

42. Palmer J, Flint S, Brooks J. Bacterial cell attachment, the beginning of a biofilm. J Ind Microbiol Biotechnol. 2007;34(9):577-588.

43. Lu HP, Liu Y, Guo J, Wu HL, Wang JX, Wu G. Biomaterials with antibacterial and osteoinductive properties to repair infected bone defects. Int J Mol Sci. 2016;17(3):No. 334.

44. Gristina AG. Biomaterial-centered infection: microbial adhesion versus tissue integration. Science. 1987;237(4822):1588-1595.

45. Li ZT, Huang XH, Lin LC, Jiao YP, Zhou CR, Liu ZH. Polyphenol and Cu^{2+} surface-modified chitin sponge synergizes with antibacterial, antioxidant and pro-vascularization activities for effective scarless regeneration of burned skin. Chem Eng J. 2021;419:No. 129488.

46. Callaway DA, Jiang JX. Reactive oxygen species and oxidative stress in osteoclastogenesis, skeletal aging and bone diseases. J Bone Miner Metab. 2015;33(4):359-370.

47. Snezhkina AV, Kudryavtseva AV, Kardymon OL, Savvateeva MV, Melnikova NV, Krasnov GS, Dmitriev AA. ROS generation and antioxidant defense systems in normal and malignant cells. Oxid Med Cell Longev. 2019;2019:No. 6175804.

48. Sun SW, Huang SQ, Shi YN, Shao YT, Qiu JR, Sedjoah R, Yan ZZ, Ding LP, Zou DD, Xin ZH. Extraction, isolation, characterization and antimicrobial activities of non-extractable polyphenols from pomegranate peel. Food Chem. 2021;351:No. 129232.

49. Yang YH, Zhang T. Antimicrobial activities of tea polyphenol on phytopathogens: a review. Molecules. 2019;24(4):No. 816.

50. Zhao Y, Liu R, Fan Y, Zhao B, Qian W, Guo J, Li C, Chen S, Luo G, Deng H, Zhang J. Self-sealing hemostatic and antibacterial needles by polyphenol-assisted surface self-assembly of multifunctional nanoparticles. Chem Eng J. 2021;425:No. 130621.

51. Ki SH, Lee S, Kim D, Song SJ, Hong SP, Cho S, Kang SM, Choi JS, Cho WK. Antibacterial film formation through iron(III) complexation and oxidation-induced cross-linking of OEG-DOPA. Langmuir. 2019;35(45):14465-14472.

52. Sun HQ, Lu XM, Gao PJ. The exploration of the antibacterial mechanism of Fe^{3+} against bacteria. Braz J Microbiol. 2011;42(1):410-414.

Schemes

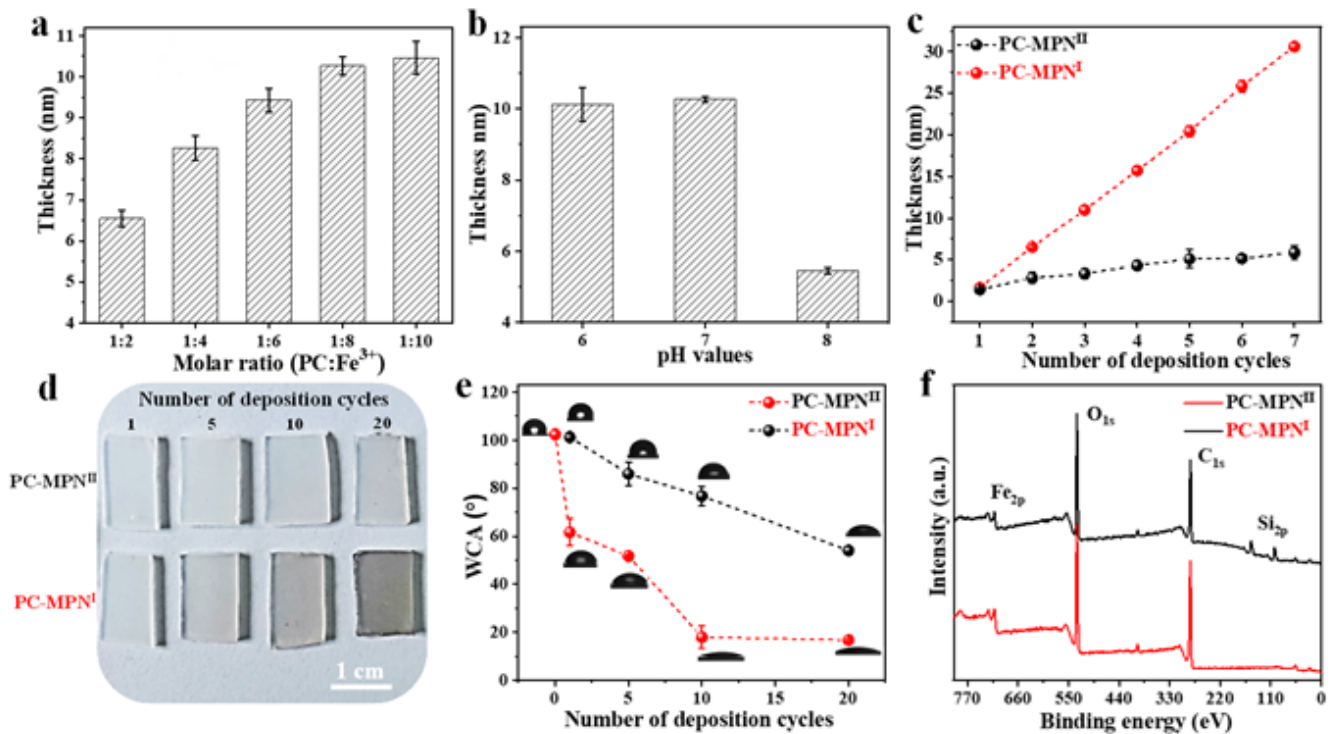Schemes 1 and 2 are available in the Supplemental Files section

Figures

Figure 1

Effect of the (a) molar ratio between PC and Fe^{3+}, (b) pH and (c) different engineering routes (route I and route II) on the thickness of the PC-MPN coating on silicon. (d) Photographs and (e) water contact angle of the PC-MPN[I] and PC-MPN[II] coatings on PP sheets with different deposition cycles. (f) XPS spectra of PC-MPN[I] and PC-MPN[II] coatings on silicon. The numbers of deposition cycles were 3 for (a) and (b) and 7 for (f).

Figure 2

(a) XPS spectrum, (b) atomic proportion, and (c) molar ratio of Fe to PC in the PC-MPN[I] and PC-MPN[II] coatings. Detailed O 1s spectra of the (d) PC-MPN[I] and (e) PC-MPN[II] coatings. (f) Proportion of O in different chemical states in the PC-MPN[I] and PC-MPN[II] coatings.

Figure 3

UV absorbance at 210 nm as a function of deposition cycles for (a) PC-MPN[I] and (b) PC-MPN[II] coatings. (c) UV absorbance at 210 nm and (d) coating thickness of the PC-MPN[II] coating before and after treatment with $Fe(NO_3)_3$ and HCl solutions. Frequency shift Δf of the PC-MPN[I] coating in (e) $Fe(NO_3)_3$ and HCl and (f) PC solutions.

Figure 4

(a) Coating thickness of the PC-MPN^{I} and PC-MPN^{II} coatings before and after treatment with Fe(NO$_3$)$_3$ for 30 min. AFM images of (b) PC-MPN^{I} and (c) PC-MPN^{II} coatings before and after treatment with Fe(NO$_3$)$_3$ for 30 min. b$_1$, c$_1$ and b$_2$, c$_2$ are images taken before and after treatment, respectively. (d) Surface roughness of the PC-MPN^{I} and PC-MPN^{II} coatings before and after treatment with Fe(NO$_3$)$_3$ for 30 min.

Figure 5

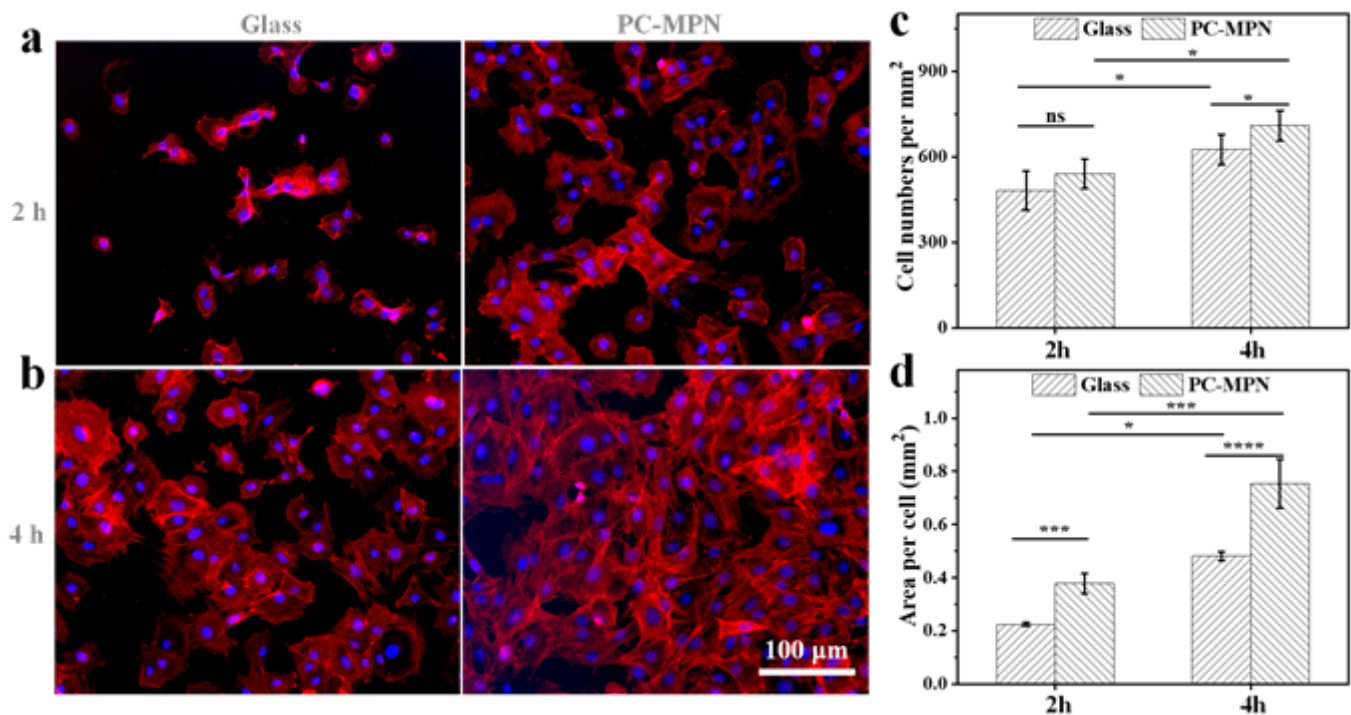Antioxidant activity of glass and PC-MPN coating as a function of stored time.

Figure 6

Adhesion of cells to the PC-MPN coating: (a-b) Fluorescence microscopy images of MC3T3-E1 cells seeded on glass and PC-MPN coating for 2 and 4 h. (c) Cell number per square millimeter and (d) area per cell of the seeded MC3T3-E1 on glass and PC-MPN coating at 2 h and 4 h.
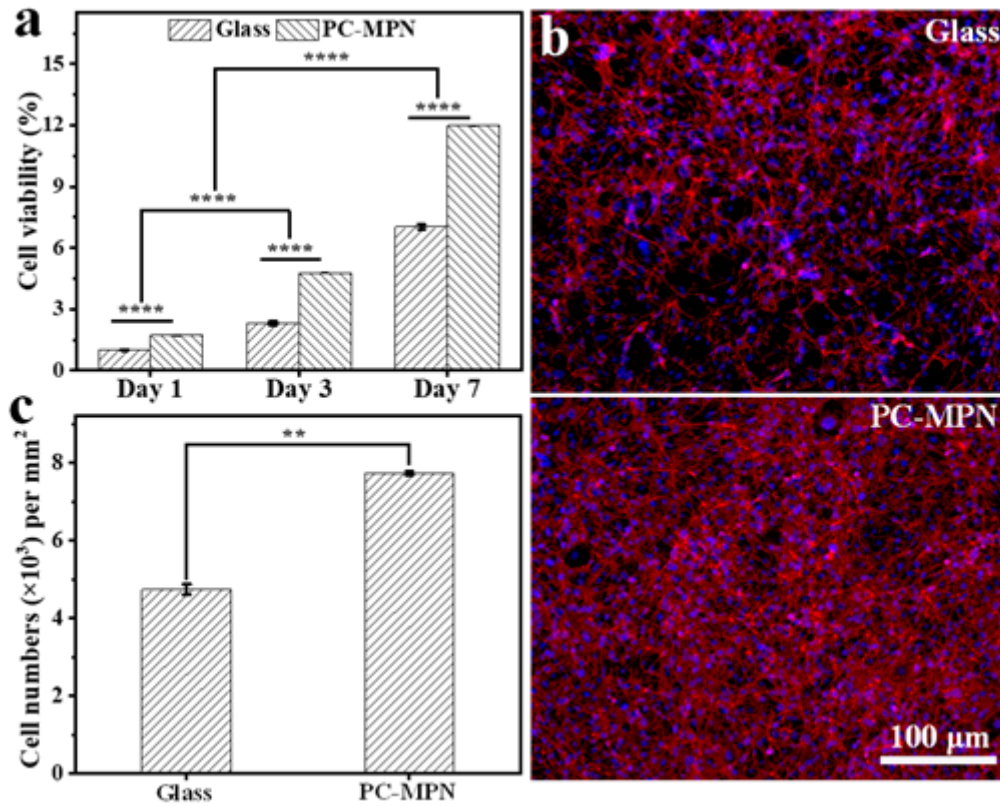
Figure 7

Proliferation of cells on the PC-MPN coating: (a) Relative cell activity of MC3T3-E1 cells seeded on glass and the PC-MPN coatings for 1, 3 and 7 days. (b) Fluorescence microscopy images of MC3T3-E1 cells seeded on glass and the PC-MPN coating. (c) Cell numbers per square millimeter onto glass and the PC-MPN coating for 7 days.
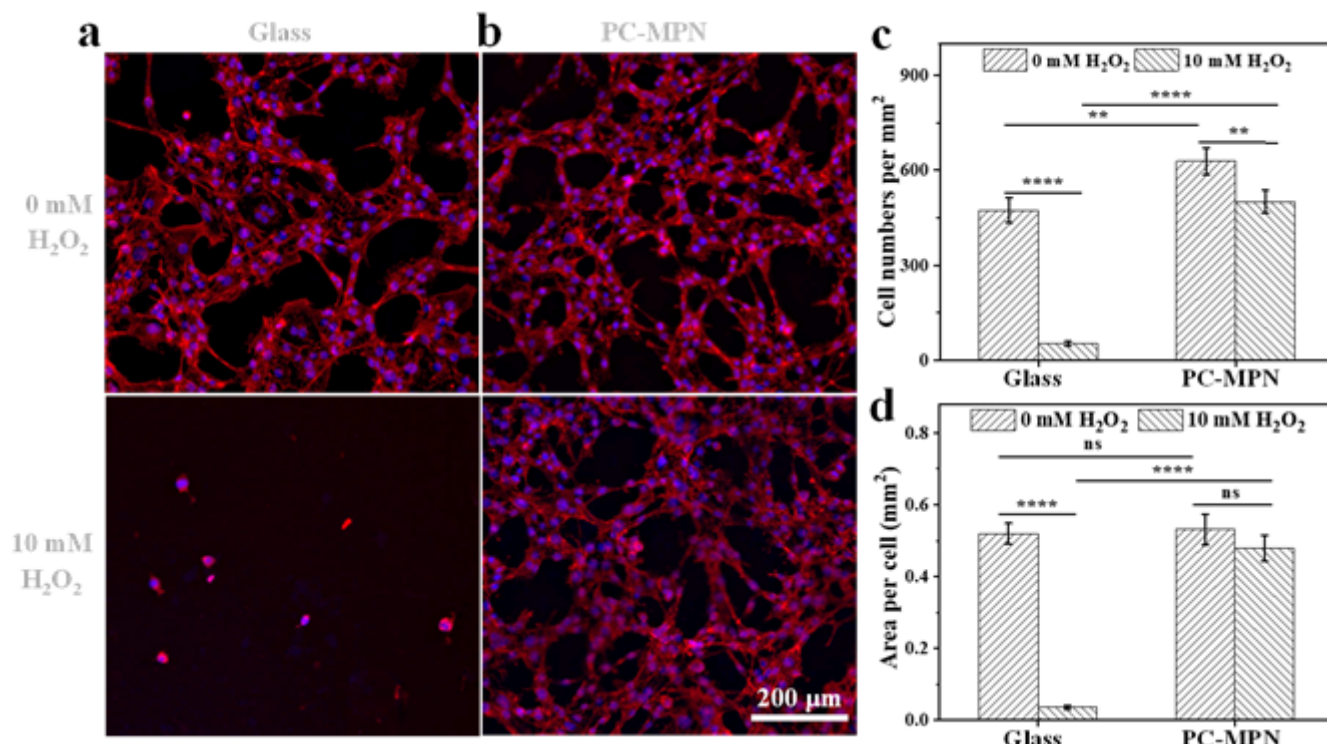
Figure 8

Antioxidant profile of the cell response: (a-b) Fluorescence microscopy images of MC3T3-E1 cells seeded on glass and PC-MPN coating. (c) Cell numbers per square millimeter and (d) area per cell on glass and PC-MPN coating before and after 10 mM H_2O_2 treatment.

Figure 9

Antibacterial properties of the coating: (a) SEM and (b) fluorescence microscopy images of *S. aureus* and *E. coli* on substrates, PC-MPN coating and PC-MPN-Ag coating.

Supplementary Files

This is a list of supplementary files associated with this preprint. Click to download.

- SIJNB.docx
- GraphicalAbstract.png
- Scheme1.png
- Scheme2.png